# Optical Line Width Broadening Mechanisms at the 10 kHz Level in $Eu^{3+}$:$Y_2O_3$ Nanoparticles - Supporting information

John G. Bartholomew,[*,†] Karmel de Oliveira Lima,[†] Alban Ferrier,[†,‡] and Philippe Goldner[†]

†*PSL Research University, Chimie ParisTech, CNRS, Institut de Recherche de Chimie Paris, 75005, Paris, France*

‡*Sorbonne Universités, UPMC Université Paris 06, 75005, Paris, France*

E-mail: john.g.bartholomew@gmail.com

# S1. Apparatus and measurement sequences

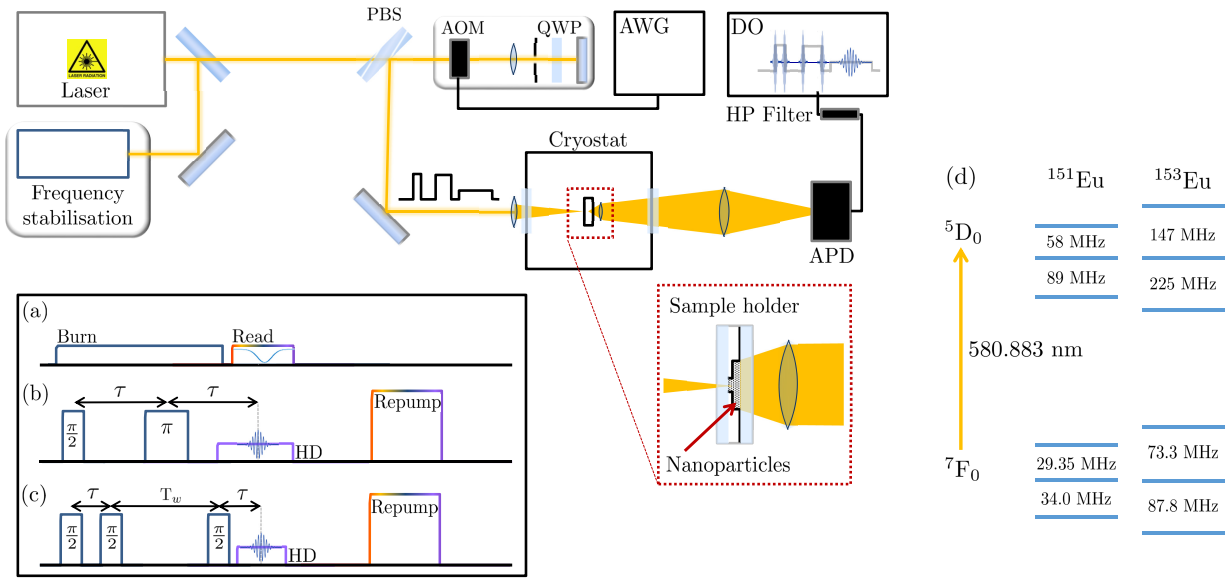


Figure S1: Apparatus for the high resolution spectroscopy of $Eu^{3+}$:$Y_2O_3$ nanoparticles. The following abbreviations have been used: AOM - acousto-optic modulator, QWP - quarter wave plate, AWG - arbitrary waveform generator, DO - digital oscilloscope, APD - avalanche photodiode, and HD - heterodyne detection pulse. The lower left inset shows the three measurement sequences used in this work: (a) hole burning spectroscopy, (b) two pulse photon echoes, and (c) three pulse photon echoes. Details on both the apparatus and the measurement sequences are given in the accompanying text. The energy level diagram for the two $Eu^{3+}$ isotopes in $Y_2O_3$ is shown in (d), where the hyperfine level splittings are from ref 1.

We excited the $^7F_0 \leftrightarrow {}^5D_0$ transition of the $C_2$ symmetry $Eu^{3+}$:$Y_2O_3$ site within 1 GHz of the central frequency of the inhomogeneously broadened distribution (shown in Figure 1 of the main text) at 516.098 THz (580.883 nm in vacuum) using a Sirah Matisse DS laser. The laser line width was of the order of 300 kHz, which was achieved by locking the laser to an external reference cavity. The intensity and frequency of the laser light was shaped by an acousto-optic modulator (AOM) with a center frequency of 200 MHz, which was aligned in a double pass configuration. The AOM driving signal was provided by an arbitrary wave generator, which was programmed through a computer script interface.

The nanoparticle powder was housed between two glass plates as shown in the inset in the lower right of Figure S1. For the zero magnetic field studies the housing was constructed from copper, whereas for the high magnetic field studies the housing was made entirely of

glass. The light was focused onto a 2 mm diameter aperture in the front of the housing using a 75 mm focal length lens, which was positioned outside the cryostat. The transmitted light and fluorescence was collected with a 5 mm lens mounted directly behind the sample holder inside the cryostat. The collected light was imaged onto a silicon avalanche photodiode and the resultant electrical signal was analyzed using a digital oscilloscope.

The inset in the lower left of Figure S1 shows the three measurement sequences used in this work. Sequence (a) was used for the hole burning measurements. A depleted spectral region (hole) was burned by a 1 ms pulse with an intensity (at the sample) of 12 mW. This is possible because the $^7F_0$ ground state of $Eu^{3+}$ possesses three doubly degenerate levels arising from the nuclear quadrupole interaction (see part (d) in Figure S1). Upon optical excitation and the resultant relaxation, there is a high probability of inducing a change in nuclear spin state. Because the other nuclear hyperfine levels are separated by many tens of MHz, if population is optically pumped to these levels it is no longer resonant with the excitation frequency. After a delay of 1 $\mu$s, the resulting spectral feature was read out by monitoring the transmitted intensity of the laser during a 500 $\mu$s frequency scan from $-25$ MHz to $+25$ MHz relative to the burn frequency. The intensity of the read pulse was equal to that of the burn. To avoid hole-shape distortion due to the repeated scanning of the same spectral region, the laser was slowly scanned over a 500 MHz region.

Sequence (b) shows the pulses used for the two pulse photon echo measurements. Photon echoes are the optical equivalent of spin echoes performed in nuclear magnetic resonance and electron paramagnetic resonance experiments. The angles labeling the pulses refer to rotation angles on the Bloch sphere. The $\pi/2$ pulse drives the ensemble into a 50:50 coherent superposition of the ground and excited state levels. This initial coherence quickly decays due to the frequency-dependent phase precession of each ion. After a delay $\tau$, a $\pi$ pulse is applied, which effectively reverses the phase precession. At a time $\tau$ after the second pulse, the ensemble has rephased and a photon echo is emitted from the ensemble. Because each ion has a finite line width $\Gamma_h$ total rephasing is not possible, which leads to an exponential

decrease in the echo amplitude as the delay is increased (see the inset of Figure 4 in the main text).

Three pulse photon echoes, the sequence for which is shown in (c), are an extension of the two pulse echo. The second $\pi/2$ maps the ensemble coherence onto population, or equivalently, creates a spectral grating in frequency space. By applying a third $\pi/2$ pulse after a time $T_w$, the population difference is mapped back onto a coherence, which then rephases. Initially, the frequency grating created after the second pulse is preserved because the optical population lifetime $T_1$ is approximately 1 ms for the studied sample. Once $T_w$ becomes long relative to $T_1$, the grating can still be partially preserved because ions that were in the excited state can decay to non-resonant hyperfine ground states. By mapping the amplitude of the three pulse echo as a function of $\tau$ at a fixed $T_w$, the effective line width can be measured for perturbations acting on a time scale equal to $T_w$.

For both the two pulse and three pulse photon echo measurements, the echo amplitude was measured using heterodyne detection. An additional pulse was applied to the sample coincident in time with the ensemble rephasing. The intensity of the heterodyne detection pulse was a factor of three less than the $\pi/2$ and $\pi$ pulses and was frequency shifted by +40 MHz. The echo signal interferes coherently with the heterodyne pulse resulting in a 40 MHz beat signal. This is easily isolated using a high pass electronic filter and the Fourier transform utility on the oscilloscope.

To avoid optically pumping all resonant ions to a non-resonant hyperfine ground state, ten chirped pulses were applied to the sample in between each echo measurement. The intensity of these pulses was at most 50% larger than the excitation pulses, and the frequency chirp extended over −100 MHz to +100 MHz. These pulses optically pump the ions such that the distribution of population between the ground states is the same for every measurement. This allows the echo pulse frequency to be fixed at the one position within the inhomogeneous line width.

## S2. Estimation of Rabi frequency

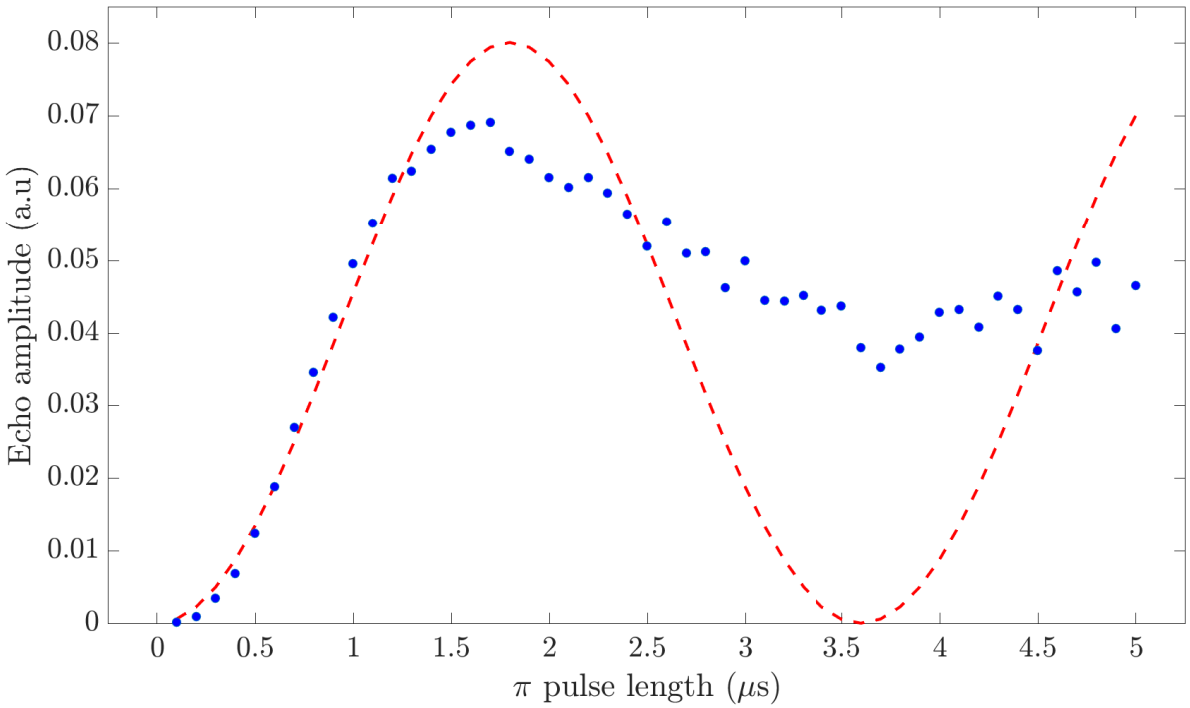


Figure S2: The echo amplitude as a function of the $\pi$ pulse length at a delay $\tau = 3$ $\mu$s for an excitation power of 120 mW. The filled blue circles are the experimental data. The dashed red curve is a theoretical fit to the data (see ref 2) for a homogeneous ensemble driven with a Rabi frequency of $2\pi \times 278$ kHz (fitting points for which ($\pi$ pulse length) $< 1.5$ $\mu$s).

Figure S2 shows the variation in echo amplitude as a function of the $\pi$ pulse length. For this data set, the $\pi/2$ pulse was fixed at a length of 0.9 $\mu$s with an excitation power of 120 mW, and the delay was also fixed at $\tau = 3$ $\mu$s. The excitation power for the $\pi$ pulse was 120 mW. The echo amplitude initially increases as the pulse area increases toward a value of $\pi$ but does not exhibit Rabi flopping because of the inhomogeneity in the $Eu^{3+}$ dipole orientations and the inhomogeneity in field amplitude across the excitation beam. The theoretical fit shown in Figure S2, is the variation in echo amplitude as a function of pulse length for a homogeneous Rabi frequency of $\Omega = 2\pi \times 278$ kHz. At this Rabi frequency a $\pi$ pulse is obtained for a pulse length of 1.8 $\mu$s. Because of the close fit of the data to the theoretical curve in the region where the length of the $\pi$ pulse $< 1.5$ $\mu$s, the pulses used in the two and three pulse echo measurements assumed an effective collective Rabi frequency

equal to $\Omega$.

From the excitation parameters for the pulsed measurements, the excitation bandwidth is certainly less than 2 MHz. For a doping concentration of 0.5% and an inhomogeneous line width of 16 GHz, this excitation bandwidth bounds the excitation density of $C_2$ site $Eu^{3+}$ ions to approximately $1.25 \times 10^{16}$ $cm^{-3}$. The instantaneous spectral diffusion (ISD) coefficient for $Eu^{3+}$:$Y_2O_3$ is reported as $1.3 \times 10^{-13}$ Hz $cm^3$ (ref 3), which sets a bound on $\Gamma_{ISD}$ of 2 kHz.

## S3. Example echo decays at differing excitation intensity

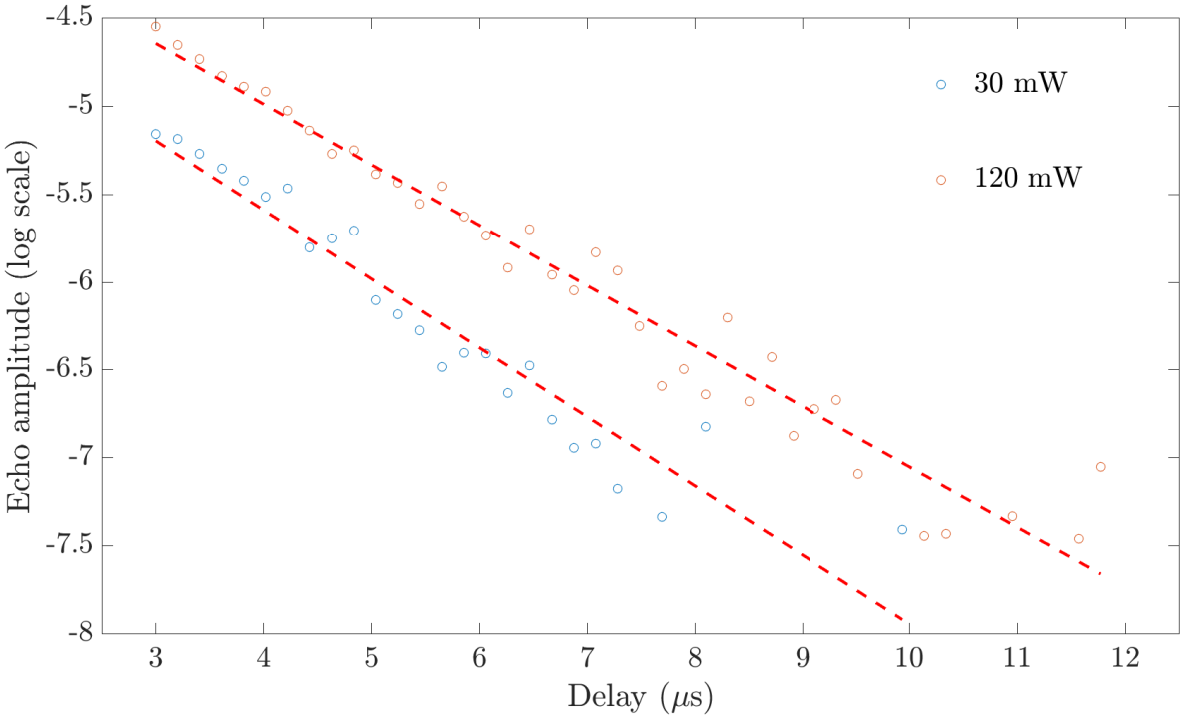


Figure S3: Echo decay curves as a function of the delay $\tau$ at excitation powers of 30 mW and 120 mW.

Figure S3 is an example of the echo decay behavior as a function of excitation power observed for the nanoparticle sample. In general, using more intense pulses to excite photon echoes resulted in slower echo signal decays as a function of delay $\tau$. In the example provided,

the respective measured line widths were $62 \pm 4$ kHz (30 mW) and $55 \pm 2$ kHz (120 mW), which were measured at a temperature of 2 K. This is strong evidence that instantaneous spectral diffusion is not the dominant contribution to the homogeneous line width under these excitation conditions. Below an excitation power of 30 mW, the signal to noise ratio of the measurement decreased significantly and the required pulse lengths to achieve the desired pulse areas were approaching the coherence time of the laser.

We attribute the observed trend to an inhomogeneity across the measured nanoparticles, which results in a distribution of line widths. The more ions that are excited yields a larger signal, which allows echoes to be observed at longer delays. The ions contributing to echoes at longer delays are those with narrower line widths. Therefore, signals that can be measured at longer delays yield a narrower effective linewidth for the ensemble.

# References


(1) Babbitt, W. R.; Lezama, A.; Mossberg, T. W. *Phys. Rev. B* **1989**, *39*, 1987–1992, DOI: 10.1103/PhysRevB.39.1987.

(2) Ruggiero, J.; Le Gouët, J.-L.; Simon, C.; Chanelière, T. *Phys. Rev. A* **2009**, *79*, 053851, DOI: 10.1103/PhysRevA.79.053851.

(3) Thiel, C. W.; Macfarlane, R. M.; Sun, Y.; Böttger, T.; Sinclair, N.; Tittel, W.; Cone, R. L. Evaluating the practical impact on applications of excitation-induced decoherence in rare-earth-doped optical materials. 2015; Quantum Light-Matter Interaction in Solid State Systems, Barcelona.